UNIVERSITY OF CALIFORNIA,
IRVINE

# Material Distortion in Laser-based Additive Manufacturing Component of PEM Fuel Cell: Numerical Analysis and Parametric Study

THESIS

submitted in partial satisfaction of the requirements
for the degree of

MASTER OF SCIENCE

in Mechanical Engineering

by

Peixin He

Dissertation Committee:
Professor Yun Wang, Chair
Professor Penghui Cao
Professor Lorenzo Valdevit

2020

## TABLE OF CONTENTS

## LIST OF FIGURES

Page

## LIST OF TABLES

## ACKNOWLEDGEMENTS

There are no proper words to convey my deep gratitude and respect for my committee chair, Professor Yun Wang, who has been the role model for pursuing the preciseness and beauty of nature science for me. He has inspired me to become an independent researcher and helped me realize the power of critical reasoning. He also demonstrated what a brilliant and hard-working scientist can accomplish. He has been supportive and offering a great platform for student like me getting into the new environment of studying abroad.

My sincere thanks must also go to the members of my thesis committee: Professors Penghui Cao and Lorenzo Valdevit. They generously gave their time to offer me valuable ideas and feedback towards the additive manufacturing field.

## ABSTRACT OF THE THESIS

Material Distortion in a Laser-based Additive Manufacturing Component of Fuel Cell: Numerical Analysis and Parametric Study

by

Peixin He

Renewable Energy Resources Lab (RERL)

Department of Mechanical and Aerospace Engineering,

University of California, Irvine, 2020

Professor Yun Wang, Chair

Laser powder bed fusion (LPBF), as a popular additive manufacturing (AM) technique, has gained a great deal of research attention and industrial application. Its capability of producing complicated shapes and structures enables this technique to be favored for manufacturing critical prototypes and complex parts. Meanwhile, LPBF techniques also have significant advantages over many other AM processes that is they do not require support structure which allows more interest in producing parts with higher complexity since overhangs and unconnected islands are supported by surrounding unfused powder bed instead. However, in fabrication, the constant melting and cooling of metal powders by layers leads to a large gradient and rapid evolution of temperature, causing considerable residual stress and deformation. Fuel cells are widely regarded as a promising candidate as the next-generation energy device, which electrochemically converts the chemical energy in the injected fuel, such as hydrogen gas, directly to electricity. Fuel cell components are required to be free of distortion to avoid leakage of reactant gases and contaminants and interfacial

resistance. In this study, a three-dimensional thermal analysis model is employed to numerically study the residual stress and deformation in the LPBF fabricated inlet/outlet of a fuel cell that connects to its bipolar plate. Inconel 718 and stainless steel SS316L are used as the powder materials, respectively. The results of distortion are validated against both experimental and other modeling data. Additionally, the validated tool is employed to investigate several major parameters in LPBF fabrication and their impacts on distortion, including the laser power, laser speed, and layer thickness. It is found that the laser power and speed have a significant impact on the distortion of the pipe wall, while the scan pattern shows little influence. Additionally, SS316L shows a much less distortion (about 40 μm) than that of In718 which is about 90 μm for the maximum distortion and a nearly 30% smaller average distortion at all measuring locations.

# INTRODUCTION

Additive manufacturing (AM), as an important advanced manufacturing method, has successfully been employed to fabricate a wide variety of products. Metal AM technology uses a high-density energy beam heat source to realize the layer-by-layer fabrication of metal components by melting powders. Several metal AM methods, such as Selective Laser Melting (SLM), Electron Beam Melting (EBM), and Laser Engineered Net Shaping (LENS), are receiving a growing attention in research and development (R&D) [1]. Laser Powder Bed Fusion (LPBF), also known as Direct Metal Laser Melting (DMLM), is a subcategory of SLM, and is able to produce prototypes directly from CAD files [2], and is one of the early commercialized AM technologies [3].

Fuel cells are electrochemical devices, which directly convert the chemical energy stored in fuels to electricity under high efficiency and low emissions. In fuel cell operation, fuel and air reactants are injected to the anode and cathode flow channel systems via the inlets, respectively, and remaining fuel, air, and products are removed out of the fuel cell via the outlets connecting to the bipolar plates. Laser-based AM technology or, specifically, LPBF, can be used to fabricate fuel cell components, such as the bipolar plates, inlet/outlet fitting, porous media flow field, and membrane. Figure 1(a) to (c) demonstrate how LENS is used to build models using SS316L powders.

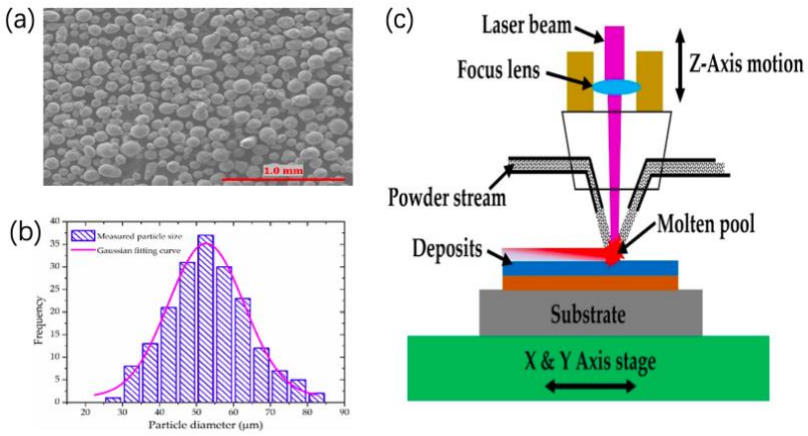


Figure 1. (a) SS316L powder feedstock; (b) Particle size distribution of the SS316L powders; and (c) Schematic diagram of laser-based AM fabrication process using laser engineered net shaping (LENS) as example [4].

In fuel cells such as polymer electrolyte membrane (PEM) fuel cells and solid oxide fuel cells (SOFCs), reactants may operate under a pressurized condition to reduce the concentration loss. Thus, their components need to be free of major distortion in fabrication to avoid assembly mismatch, reactant leakage and contaminant intrusion. Figure 2(a) shows an experimental PEM fuel cell with the inlet/outlet on the bipolar plate (BP). The core parts of a single PEM fuel cell can be fabricated as thin as 1-2 mm with the PEM, CLs, diffusion media, and BPs around 0.02, 0.01, 0.2, and 1 mm, respectively [5] [6] [7] [8] [9] [10] [11]. However, as shown in Figure 1(c) the bulky mechanical support plates need to be added to assemble the core parts of fuel cells and hold fittings to connect with hydrogen and air lines, which considerably reduces fuel cell power density, especially for single fuel cell or small stacks. LPBF technology is advantageous in fabricating multiple fuel cell components together with integrity, reducing additional parts for cell assembly and connection, as shown in Figure 2. In addition, the microstructures of porous components of

PEM fuel cells such as the porous media flow field [12] [13] [14] [15] [16] and even gas diffusion media [17] [18] [19] [20] [21] can be digitally designed and 3D printed by LPBF.

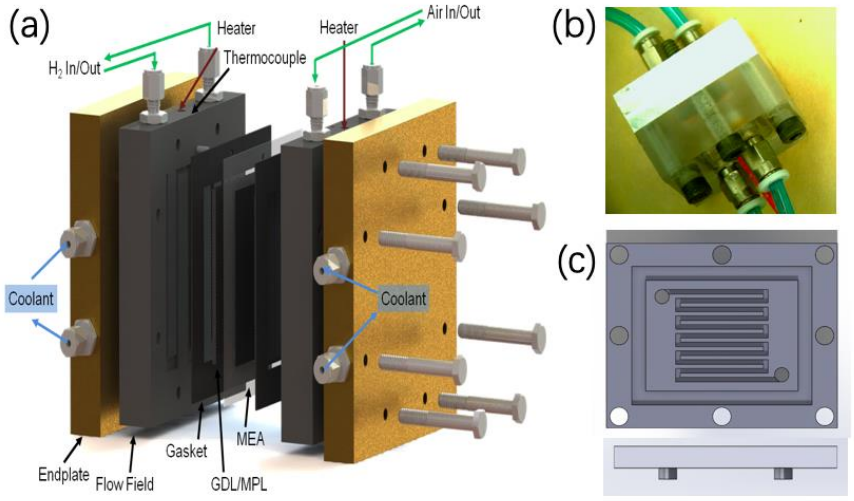


Figure 2. (a) An experimental PEM fuel cell and its inlet/outlet fittings on sides [22]; (b) A small PEM fuel cell with a 1 $cm^2$ MEA [23]; (c) Design of a 3D printing bipolar plate (BP) with the side view of the 3D printing plate with inlet/outlet fittings on the BP.

In the AM fabrication, large thermal gradients and nonhomogeneous cooling rates near the molten pool induce considerable thermal strains [24, 25], which will build up residual stresses and deformations in the final product. Novar et al. [26] investigated the effects of laser input power on AM products, showing that high power could yield non-uniform shrinkage and curling of final parts while low power could cause weak and partial sintering of powder bed. In addition, undesirable effects could be avoided and mitigated by setting more suitable parameters in given working conditions for specific building parts. Zhang et al. [4] employed a LENS system to fabricate a SS316L rod, which exhibits a compressive residual stress of -197.4 MPa. Their SEM images showed the layered and molten-pool footprints and dendritic grain growth in the building

direction. Thermal annealing was shown to significantly reduce the residual stress of the as-printed product. In practice, AM processes are usually operated under experience-based optimized pre-setting to reduce any unexpected stresses and distortions [27]. To investigate AM process in detail, Leung et al. [28] employed in-situ X-ray imaging technique to reveal the underlying physical phenomena during the deposition of the first and second layer melt tracks. They showed laser-induced gas jets cause the formation of melt tracks and denuded zones by spattering and indicated the mechanisms of pore migration by temperature-gradient-driven Marangoni flows, pore dissolution and dispersion by laser re-melting. Martin et al. [29] used in-situ X-ray imaging and physical modeling to elucidate the mechanism of pore formation and liquid/solid interface dynamics during laser powder bed fusion. They explained that pores may form during laser scan speed change due to the rapid formation then collapse of deep keyhole depressions in the surface. They also developed mitigation strategy to eliminate pore formation and improve the AM quality. Gouge et al. [30] discussed the thermal and mechanical equations for numerical analysis of AM processes and a few issues in the numerical methods and implementation, including the boundary conditions, model of material addition, temperature-dependent properties, meshing and validation. Bikas et al. [27] discussed an AM-driven design framework which ensures full exploitation of the AM design capabilities. The design framework avoids manufacturing issues of certain geometries in conventional manufacturing, and exploits the full design-freedom potentials for AM. RÜhmer et al. [31] redesigned the first stage ring segment in a large gas turbine for SLM using IN939 to reduce the cooling air consumption and to increase the gas turbine efficiency. The design was assessed the mechanical integrity, such as low cycle fatigue (LCF), high cycle fatigue (HCF) and creep, using 3D finite element analysis (FEA) and over 2.5 million quadratic tetrahedral elements. Maksimov et al. [32] discussed ANSYS in studying the physical process of SLM with a goal to

create a set of mathematical models and user environment based on the ANSYS FEA system solver. They showed the capability of numerical prediction of manufacturing and residual stress fields formation and displacements in the SLM process. Mayer et al. [33] evaluated the ANSYS Additive Print and ANSYS Additive Suite for SLM AM, including validation in terms of residual deformation. They showed that the former is more accessible and yields accurate results within the calibrated regime, while the latter features a sounder physical basis and therefore allows for a more robust extrapolation. Dunbar et al. [34] employed LPBF to build two parts of Inconel 718 cylindrical geometry using a rotating and a constant scan patterns, respectively, to investigate post-build distortion. They also used a FE model to predict the distortion and compared favorably with their experimental measurement.

Though serval attempts have been made numerically to investigate material distortion in AM builds, few provided detailed validation against experimental data, such as distortion profiles, and applied the validated tool to carry out extensive parametric study to assess the impacts of major AM parameters on distortion for fuel cell components. In this study, we carried out a 3D numerical study, using the ANSYS Additive Suite, to investigate the material distortion of a LPBF built inlet/outlet fitting on the fuel cell bipolar plate, as shown in Figure 3. Both IN718 and SS316L are used as the building materials, respectively (The selected material chemical compositions are listed in Table 1). The results are validated against the literature experimental data in terms of distortion profiles at four directions. AM parameters, including the laser speed, laser power, layer thickness and scan strategies, on distortions are investigated. The potential impacts of distortions on fuel cell operation are discussed.

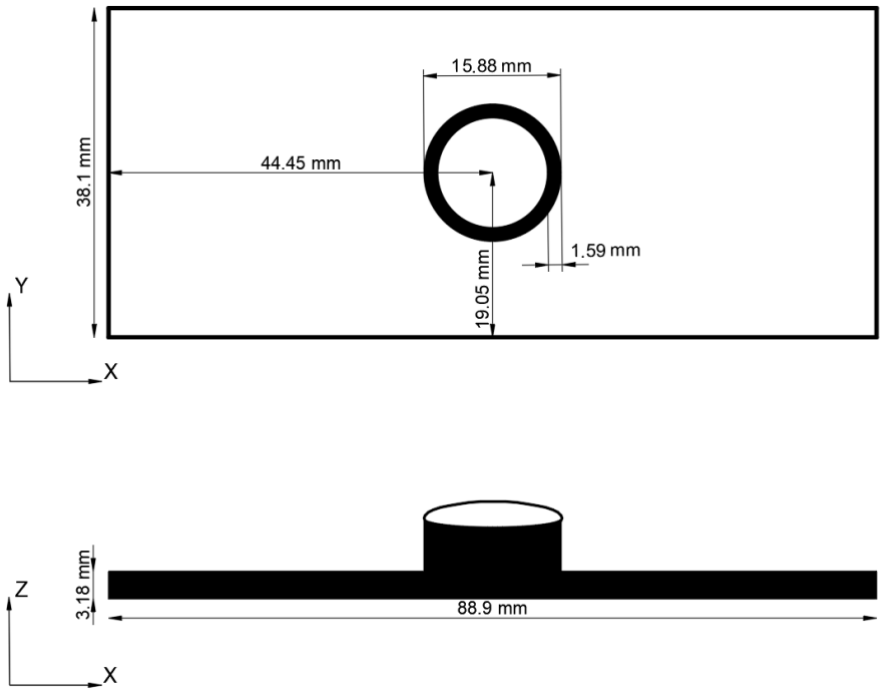


Figure 3. Schematic diagram of building part.

**Table 1**. Chemical composition of IN718 and SS316L (wt. %).

**IN718**

| Fe | Cr | Ni | Mo | Mn | Si | C | Co | P | S | Nb | Ti | Al |
|---|---|---|---|---|---|---|---|---|---|---|---|---|
| 17 | 17-21 | 50-55 | 2.8-3.3 | .35 max | .35 max | .08 max | 1.00 max | .015 max | .015 max | 4.75-5.50 | .65-1.15 | .20-0.80 |

**SS316L**

| Fe | Cr | Ni | Mo | Mn | Si | C | N | P | S |
|---|---|---|---|---|---|---|---|---|---|
| Bal. | 16.00-18.00 | 10.00-14.00 | 2.00-3.00 | 2.00 max. | .75 max. | .03 max. | .10 max. | .045 max. | .03 max |

# Chapter 1: Background of PEMFCs and AM

## 1.1 PEM Fuel Cells

PEM (Polymer Electrolyte Membrane) fuel cell is a device that converts the chemical energy from a fuel into electricity through a chemical reaction with oxygen or another oxidizing agent. PEM fuel cells have received extensive attention for its high efficiency in energy converting and emission reduction that are considered as an essential role in next energy revolution. Typically, a PEM fuel cell has a water based, acidic polymer membrane as its electrolytes, with platinum-based electrodes. As shown in Figure 4, the protons pass through the membrane to cathode side of the cell while the electrons travel in an external circuit, generating the electrical output of the cell. The overall reaction that involves in this process is: $H_2 + \frac{1}{2}O_2 \rightarrow H_2O$, with conducting iron $H^+$.

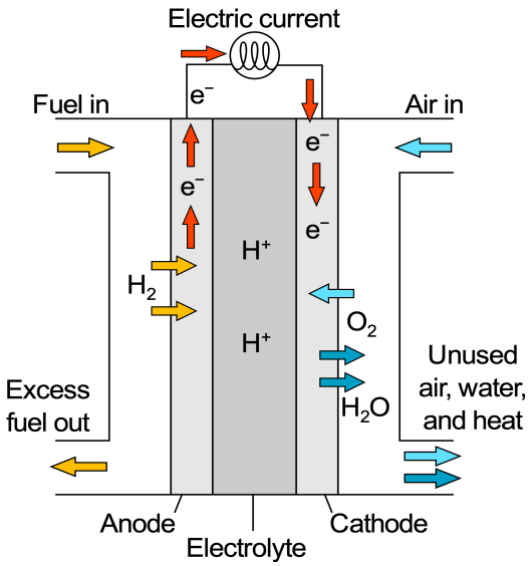


Figure 4. Vector diagram of PEM and FC operation

Hydrogen gas, methanol, alcohol and glucose are all capable to be fuels for PEM fuel cells [35], whereas Hydrogen gas is pervasively applied in industries for its rapid reactivity. In operation

process, gas flow channels (GFCs) of cathode and anode are fed with hydrogen gas and air, and then hydrogen and oxygen are electrochemically diffused to catalyst sites [35]. Since it does not involve any combustion, the efficiency of energy converting is not decided by Carnot Cycle, thus a much higher conversion rate is achieved at relatively low operation temperature.

Figure 5 displays the essential hardware components in PEM fuel cells are catalyst layers (CLs) and gas diffusion layers (GDLs) where gas transports through. Hardware include gaskets, which provide a seal around the MEA to prevent leakage of gases, and bipolar plates (BP), which are used to assemble individual PEM fuel cells into a fuel cell stack and provide channels for the gaseous fuel and air. One of the technical issues of PEM fuel cells is thermal and water management, which is delicately discussed by Wang et al. [35]. In short, hydrating the electrolytes so that reducing ionic resistance has certain conflicts with avoiding excessive liquid water so that improving mass transportation.

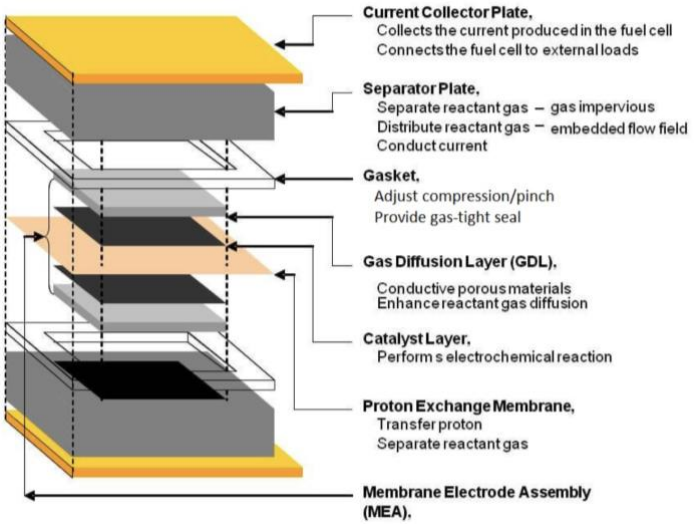

Figure 5. Diagram of PEM fuel cell hardware [36].

## 1.2 Additive Manufacturing

As introduced in pervious sections, additive manufacturing is able to deliver parts of very intricate and complex geometries with a minimum need for post-processing, so that it has massive

advantages over subtractive manufacturing methods in terms of precision fabrication and production time-shorten. Namely, AM gives as much freedom of design as possible for product designers and engineers. Forty years after its development since 1980s, this technology has been applied in various industries and researches, such as automotive, medical, electronics, aerospace and the like [37], it is foreseeable that in coming eras, AM will continue expanding market shares in above fields while exploring more appliable divisions.

AM, based on the material processed, could be divided into six major types, metal matrix, metallic alloys, ceramic matrix, polymer matrix, structural composites and nanocomposite, each of these has their suitable scenarios. Besides, Table 2 summarizes current seven AM methods and their brief characteristics by ASTM F42 Committee [38].

Table 2. Additive Manufacturing Categories defined by ASTM F42 Committee.

| **Category** | **Description** |
|---|---|
| Binder Jetting | Liquid bonding agent deposited to join powder |
| Material Jetting | Droplets of build materials selectively deposited |
| Powder Bed Fusion | Thermal energy selectively fused regions of powder bed |
| Directed Energy Deposition | Focused thermal energy melts materials as deposited |
| Sheet Lamination | Sheet of material bonded together |
| Vat Photopolymerization | Liquid photopolymer. selectively cured by light activation |
| Material Extrusion | Material selectively. dispended through nozzle or orifice |

Laser power bed fusion (LPBF), as an emerging technology among powder bed fusions, it has gained more interests for lower technological complexity and less production time resulting in lower capital investment and production costs [39]. Figure 6 prescribes the working principle of

LPBF, melting and fusion of material is obtained layer-by-layer, new powder is continuously melting by laser with an immediate solidification as soon as laser moves to neighboring portion. The final part is an ensemble of micron-size welding lines overlapping in the horizontal plane and superimposed in the vertical plane.

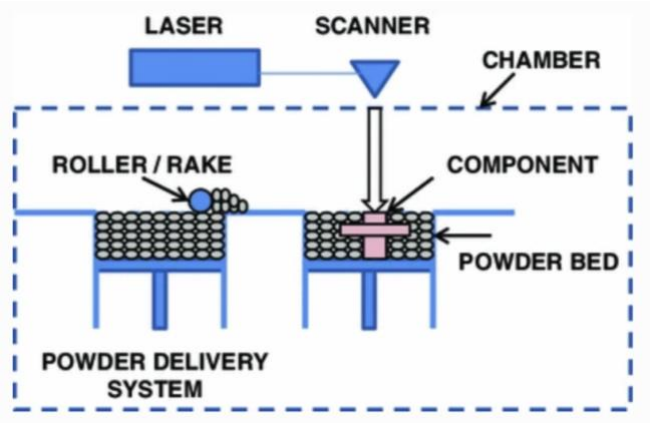


Figure 6. Schematics of a generic laser powder bed fusion system [1].

Nevertheless, there are also existing challenges that need to be optimized, such as distortions, cracks and delamination caused by high level residual stresses; discontinuous scan tracks, balling and other defects caused by incomplete fusion; micro surface roughness caused by partially sintered metal particles [39].

### 1.3 Motivation

To explore more potential application of AM or, specifically, LPBF into the usage of coming energy revolution, providing a potential solution to the rapid growing need of fuel cell production and improvement, validation and process research are studied based on a PEMFC water/air channel. A functional inlet/outlet component ensures the stable and uniform air or water flow, which plays a fundamental role within fuel cells as well as a confirmation of combing AM and cell production.

# Chapter 2: Method

## 2.1 LPBF in AAS

To investigate the distortion of AM inlet/outlet on the bipolar plate (BP), we consider a short pipe fabricated on the center of a plate, diameters as shown in Figure 3 (a), (b). For validation purpose, we follow the same dimension as the pipe in the experiment [34]. The model has a bipolar plate (BP) with a dimension of 88.9 mm×38.1mm×3.18 mm and a hollow cylinder centered on the top of the BP. The outer and inner diameter of the hollow cylinder are 15.88 mm and 12.70 mm, respectively. The build height that refers to the height of hollow inlet/outlet part above the BP, is 6.16 mm for case 1 and 12.70 mm for case 2, other parameters remain the same. To conduct future analysis and assessment of stress and distortion, the model was simplified to have constant geometric features along the height dimension. The schematic of the validation model is shown in both Figure 7 (a) and (b) , the highlighted four red lines in Figure 7(a) indicate the measurement locations (X+, X-, Y+, Y-) for both cases, and the 3D coordinate system is set with the center of the inlet/outlet on the top BP surface. The mesh used for the simulations are shown in Figure 7(b).

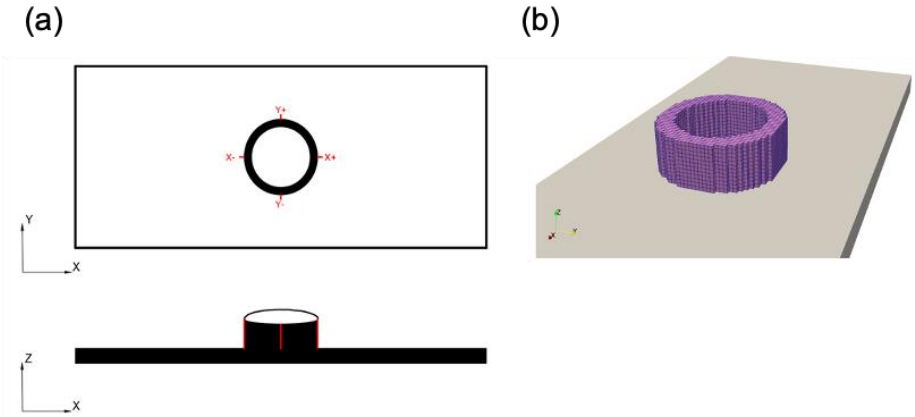


Figure 7. Measurement locations of the building part

In AAS, the mesh size was decided by voxel size and voxel sample rate. For the consideration of time and accuracy, voxel size 0.5mm was used to adequately capture part features while saving unnecessary voxelization time. In Figure 8, voxel size and sample rate effects are demonstrated. The red cube in Figure 8 (a) shows a single voxel and the yellow line represents the size of it, (b), (c), (d) show how sample rate controls the number of subvoxels. The sample rate of 5 could improve the accuracy when there is any portion of the part goes through a subvoxel, it is counted as filled. Then the voxel density for this entire voxel will be determined by the ratio of the filled subvoxels and total subvoxels. That is, if 70 subvoxels are filled in this case then the material properties in the solution are scaled down to 70/125=56% for this individual voxel. Moreover, the number of voxelization layers for case 1 would be the total height (3.18mm+6.16mm=9.34mm) divided by voxel size (0.5mm), that is approximately 19 layers we will get in the ultimate result. However, the printing layers that have different meaning as voxelization layers, are only depended on the input layer thickness and total model height. For example, if input layer thickness is 40μm, then the total number of printing layers will be about 233 layers for case 1.

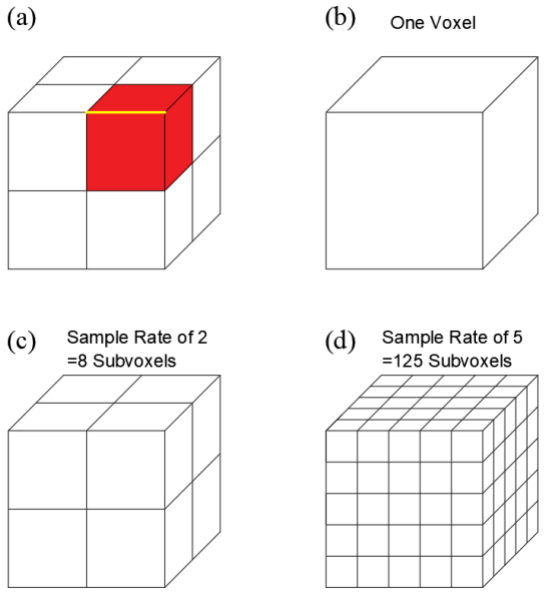


Figure 8. Schematic of voxelization method

Scan patterns are set to rotating scan for case 1 and constant scan for case 2. Figure 9(a) shows an internal scan path of a working laser beam during the printing process on a single layer. Different scan patterns are achieved by setting different values for the start angle and layer rotation angle. The rotating scan pattern has 0° and 120° as start angle and layer rotation angle; the constant scan pattern has 0° and 180° as start angle and layer rotation angle. Figure 9(b) indicates pathways of laser beam on a single layer, it helps to visualize variables that together decide the final scan strategies, such as layer thickness, hatch spacing, stripe width, start angle, layer rotation angle and the like.

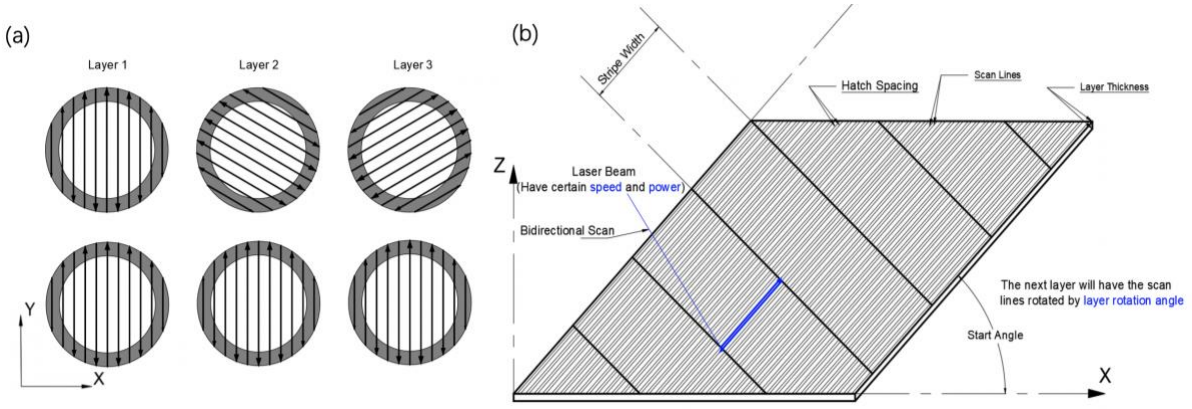


Figure 9. Pathway of (a) different scan patterns, (b) single working laser beam

The material for the fuel cell channel and BP is Inconel 718. AAS has pre-defined material property values at different temperature ranges that need to be considered, as the fact of temperature dependency of these material properties and the fluctuating temperature of melting and cooling cycles. The temperature dependency of elasticity modulus, thermal expansion coefficient, material yield strength for Inconel 718 are listed in table 3.

**Table 3.** Temperature dependent material properties of Inconel 718 [40] [41].

| Temperature [℃ ] | Elastic Modulus [GPa] | Material Yield Strength [MPa] | Thermal Expansion Coefficient [$10^{-6}$/℃] |
|---|---|---|---|

| | | | |
|---|---|---|---|
| 21 | 208 | - | - |
| 93 | 205 | 1172 | 12.8 |
| 204 | 202 | - | 13.5 |
| 316 | 194 | - | 13.9 |
| 427 | 186 | 1089 | 14.2 |
| 538 | 179 | 1068 | 14.4 |
| 649 | 172 | 1034 | 15.1 |
| 760 | 162 | 827 | 16.0 |
| 871 | 127 | 286 | - |
| 954 | 78 | 138 | - |

### 2.2 Thermal & Mechanical analysis

The thermal history is decided by performing a three-dimensional (3-D) transient thermal analysis. The heat transfer governing equation is given by [42] [41]:

$$\rho C_P \frac{dT}{dt} = \nabla \cdot (k \nabla T) + Q_r \tag{1}$$

$\rho$ is the density of the material, $C_P$ is the temperature dependent specific heat capacity, $T$ is the temperature, $t$ is time, $Q_r$ is the volumetric internal heat generation rate, $x$ is the relative reference coordinate, and $k$ is the thermal conductivity. Note that density, capacity, and thermal conductivity are all a function of temperature. $Q_r$ can be approximated by a moving heating source with a heat flux following the Gaussian distribution [41]:

$$Q_r = \frac{2P}{\pi r_0^2 H}(1 - \frac{z}{H})\exp\,(1 - \left(\frac{r}{r_0}\right)^2) \tag{2}$$

where $Q_r$ is the input energy density (W/mm$^3$), P the absorbed beam power ($W$), and $r_0$, $H$, $r$, and $z$ are parameters regarding the size and penetration of a laser beam.

The cooling at the build surface is via the thermal radiation $q_{rad}$ and convection $q_{conv}$. The flux of the former is given by:

$$q_{rad} = \varepsilon\sigma(T_s^4 - T_\infty^4) \tag{3}$$

where $\varepsilon$ is the surface emissivity, $\sigma$ is the Stefan-Boltzmann constant, and $T_s$ is the surface temperature of the building piece.

The latter is given by the Newton's law of cooling:

$$q_{conv} = h(T_s - T_\infty) \tag{4}$$

where $h$ is the convective heat transfer coefficient.

The spatial and temporal temperature variations lead to thermal distortion and consequently materials failure. It has been established that thermal distortion is affected by several AM conditions and can be evaluated using strain parameter (ε∗) [34] [41]:

$$\varepsilon^* = \frac{\beta \nabla T}{EI} \frac{t}{F\sqrt{\rho}} H^{3/2} \tag{5}$$

where $\beta$ is the volumetric expansion coefficient, $\Delta T$ the difference between the peak and ambient temperatures, t the total AM time, $H$ the heat input per unit length, $EI$ the flexural rigidity of the substrate, and $F$ the Fourier number.

To analyze the stress and distortion in detail, a quasi-static mechanical analysis is also performed, based on the stress equilibrium equation [42]:

$$\nabla \cdot \boldsymbol{\sigma} = \mathbf{0} \tag{6}$$

where $\boldsymbol{\sigma}$ is the stress. The mechanical constitutive law is:

$$\boldsymbol{\sigma} = \boldsymbol{C}\boldsymbol{\epsilon}_e \tag{7}$$

Total strain is $\boldsymbol{\epsilon}$, assuming small deformation thermo-elasto-plasticity, is total of:

$$\boldsymbol{\epsilon} = \boldsymbol{\epsilon_e} + \boldsymbol{\epsilon_P} + \boldsymbol{\epsilon_T} \tag{8}$$

$\boldsymbol{C}$ is the fourth-order material stiffness tensor, and $\boldsymbol{\epsilon_e}$, $\boldsymbol{\epsilon_P}$, $\boldsymbol{\epsilon_T}$ are the elastic, plastic, and thermal strain, respectively.

# Chapter 3: Model Validation

## 3.1 Introduction to literature experimental data

For both case 1 and case 2, 25℃ of ambient temperature, 280W of laser power, 960mm/s of scan speed, 40μm of layer thickness and 110μm of hatch spacing are chosen in experiment and other simulations. The scan patterns are rotating scan and constant scan for case 1 and case 2, respectively. Distortion data is extracted at same measurement locations for all building models, and experiment results are averaged in in groups of 10 with the standard deviation indicated by error bars [34].

## 3.2 Distortion results comparison

Figure 10 compares the distortion predictions with the experimental measurements and other simulation results at the four measuring locations for both case 1 and case 2. It can be seen that the predictions of the present study agree very well with other simulation results with acceptable match achieved for the experimental data. The discrepancy between the simulation curves and experimental data is likely caused by surface roughness, which was ignored in the numerical models, as also pointed out by Dunbar et al. [34]. The surface roughness variance can be related to scan direction, gas flow and wiper movement [43], and other processing parameters [44]. To achieve the comparison, the material properties of the Elastic Modulus, yield strength and thermal expansion coefficient are set to 179 GPa, 1127 MPa and $12.8\times10^{-6}$/℃, respectively. It can be seen that case 2 shows larger maximum distortions than case 1 due to its longer length and the constant scan pattern. Their maximum distortions are about 0.011 mm and 0.09 mm, about 0.07% and 0.057% of the outer diameter 15.88 mm, which are small but may contribute a major mismatch with the

hydrogen and air lines, if not well designed, and consequent reactant leakage under 1.5 or 2 atm operating condition.

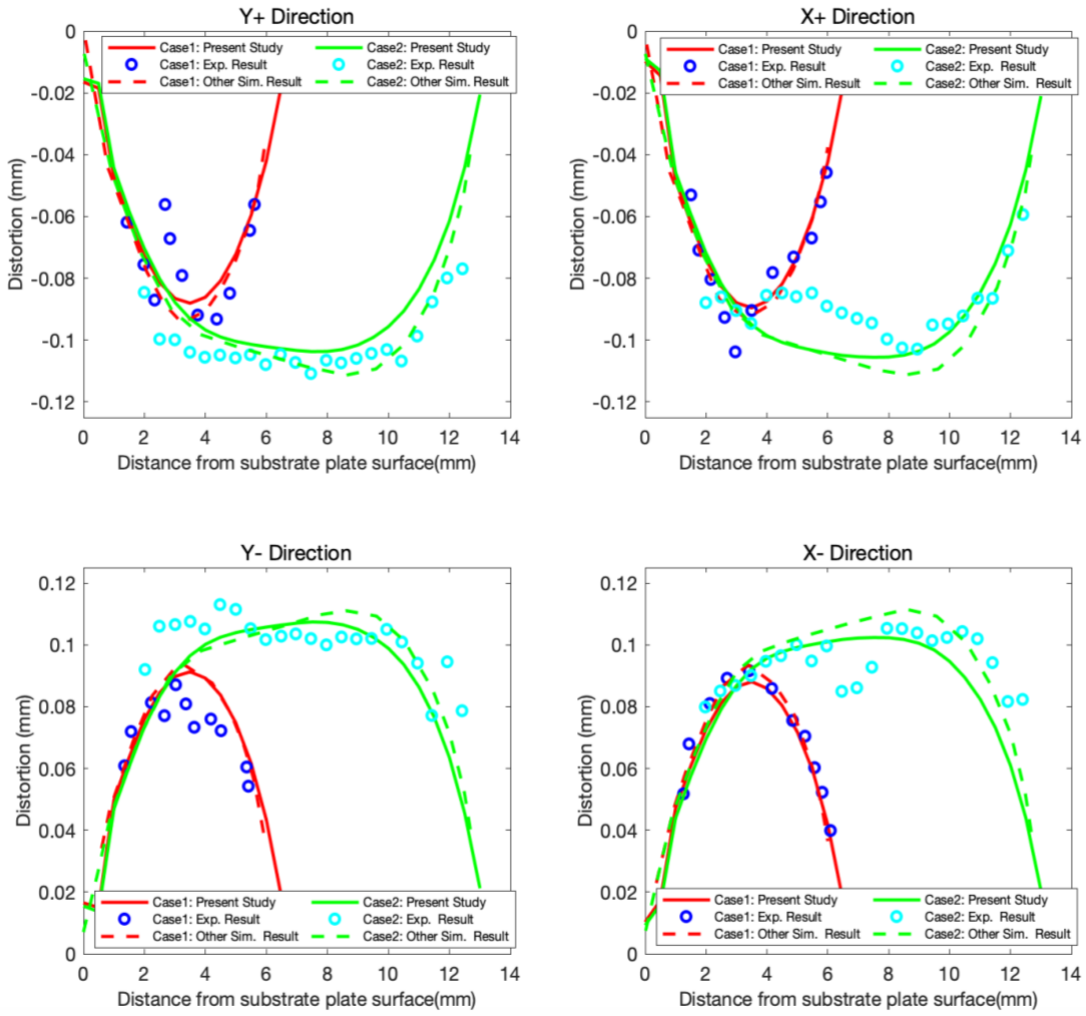


Figure 10. Comparison of distortion data at different locations for experiment measurements and validations, both case 1 and case 2. Both experimental and other simulation data are from Dunbar et al. [34].

Moreover, a quantitative comparison of deviation between validation results and experimental data was also made along the Z direction. The error rate of validation results was normalized by experimental results and averaged at each measurement location (X+, X-, Y+, Y-). Table 4 shows the averaged error rates of validation for case 1 and case 2, respectively. We can observe that the largest difference is 10.4% at Y+ direction and Y directions are larger than X directions for case 1,

which is consistent with the results in Figure 10 due to the surface defects as we discussed.

**Table 4.** Comparison of experimental measurement and validation results for case 1 and 2.

| Measurement location | Averaged error rates of case 1 (%) | Averaged error rate of case 2 (%) |
|---|---|---|
| X+ | 4.8 | 9.9 |
| X- | 5.2 | 9.5 |
| Y+ | 10.4 | 9.3 |
| Y- | 10.1 | 8.9 |

Figure 11 (a) and (b) show the predicted final builds of both cases with 10 times magnified distortion, along with distortion contours. For both cases and scan patterns, the peak distortion occurs on the middle of the cylinder build. Again, both cases present a higher degree of deformation in the middle of the build height instead of the top layers, due to the solidification and compression of pervious layers, thus require additional consideration in the fitting design of the reactant lines for perfect connection.

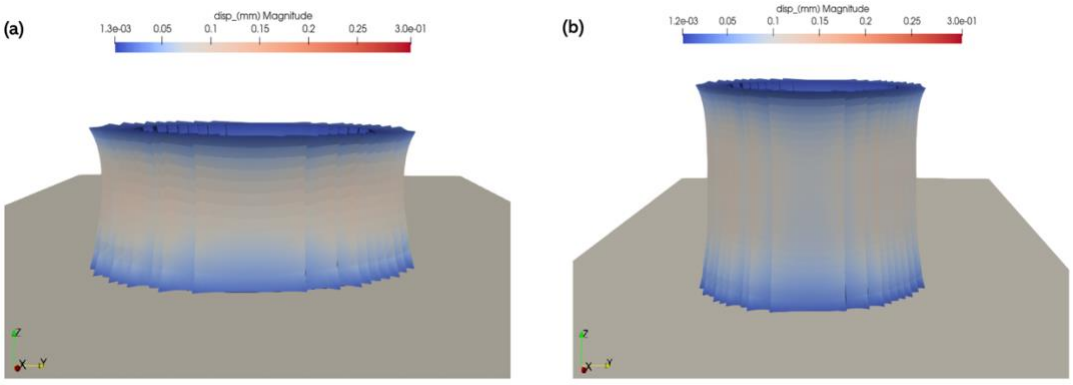


Figure 11. Predicted final geometry of (a) case 1 and (b) case 2, with 10 times magnified

To assist explaining the final shapes, Figure 12 displays the contours of the Cauchy XX and YY stresses at multiple heights of the two builds. It can be seen that the bottom and top layers are subject to tension with a stress magnitude as large as 1500 MPa. The middle the height is less

stressed though the middle part has the largest distortion, as shown in Figure 12. For each measurement location, the distortion is local minimal at top and bottom layers whereas the middle part is dominated by compressive stress, which forms a "tension to compression and then to tension" transition throughout the cylinder build. The result of it is a significant distortion occurs between multiple top and bottom layers.

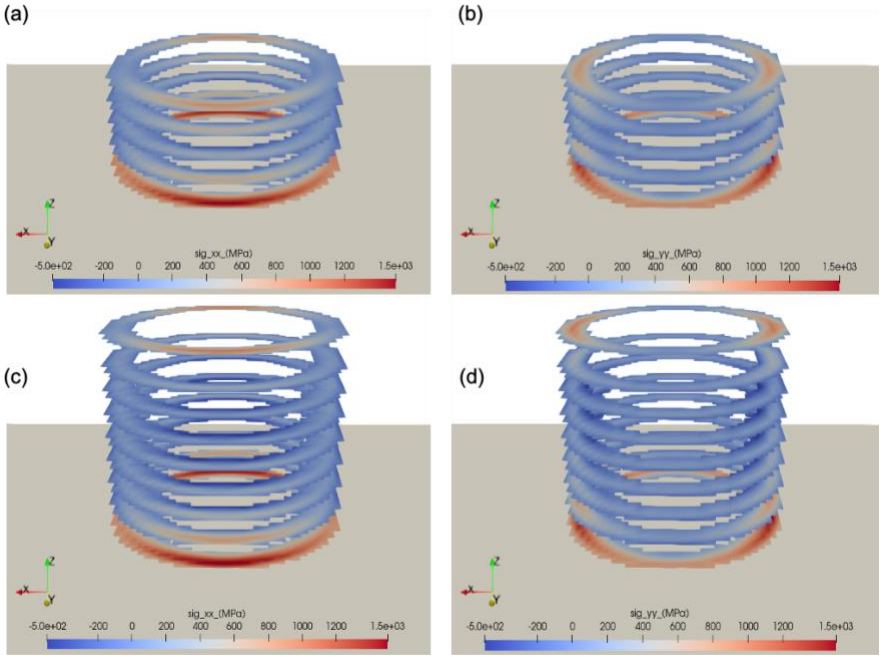


Figure 12. Cauchy XX and YY stresses at different measurement locations for (a, b) case 1 and (c, d) case 2.

## Chapter 4: Parametric study

To reveal the different impacts introduced by material variations, both material Inconel 718 and stainless 316L were used on the model from case 1 and displayed in partial directions for following study. Meanwhile, several properties and parameters, such as laser speed and power are adjusted for evaluation. Table 5 summarizes the parameters that are related to all steps in LPBF.

**Table 5.** Parameters in 3D printing.

| Types of parameters | Variables | |
|---|---|---|
| Temperature dependent material properties | • Density<br>• Thermal conductivity<br>• Specific heat | • Elastic Modulus<br>• Yield Strength<br>• Thermal expansion coefficient |
| Machine configurations | • Laser power | • Initial temperature |
| Scan strategies | • Scan speed<br>• Scan pattern<br>• Layer thickness | • Hatch spacing<br>• Stripe width |

### 4.1 Scan speed effects

Scan strategy usually refers to the scan speed, scan pattern and layer thickness. Figure 13 shows the impact of the scan speed on the distortion at X+ and Y+ locations in the range of 500 to 4000 mm/s. It can be seen that as the scan speed increases from 500 to 4000 mm/s, the distortion magnitude decreases from 0.1 to 0.07 mm for In718 and 0.05 to 0.03 mm for SS316L. This is due to the fact that decreasing laser scan speeds leads to smaller temperature gradients [45] and smaller cooling rates [46], thus lower residual stresses and distortion [47].

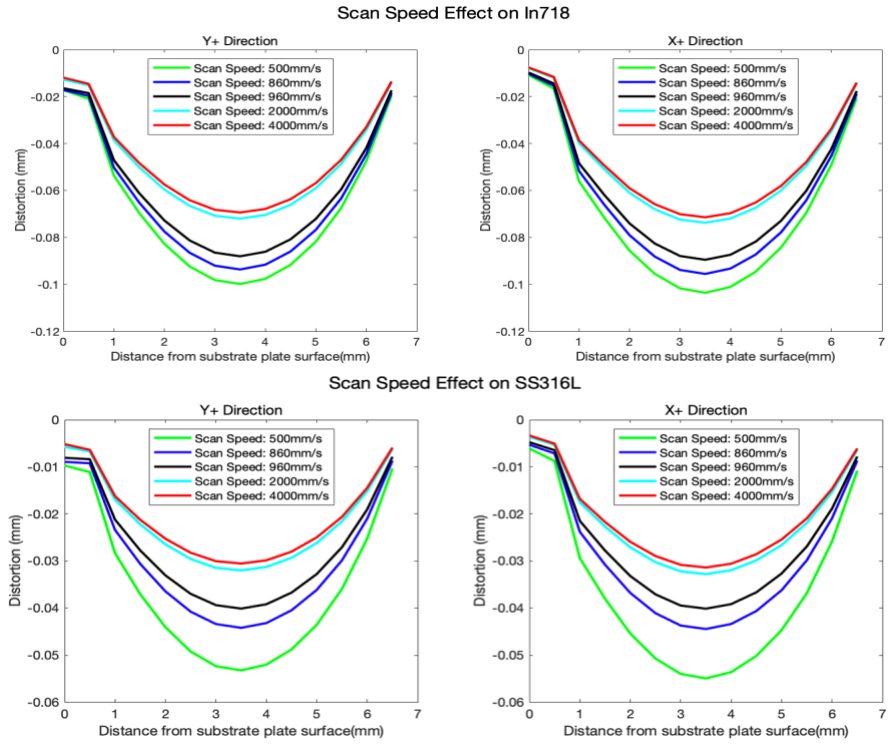


Figure 13. Parametric effect on distortion for different scan speeds.

## 4.2 Scan pattern effects

The selected scan patterns are rotating scan and constant scan, as specified in Figure 2. Figure 14 plots the distortion results for these two scan patterns on the case 1's geometry. It can be seen that the rotating scan pattern exhibits a slightly less distort than that of the constant scan in the X direction. Note that some local scan patterns may cause a significant difference on distortion [48]

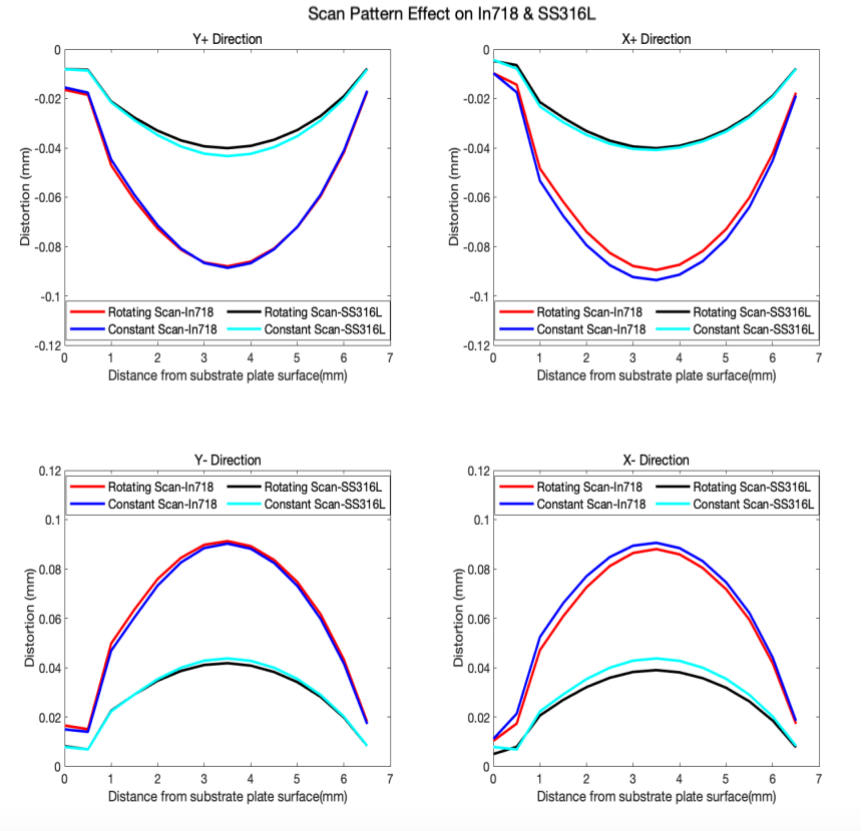


Figure 14. Parametric effect on distortion for different scan pattern.

### 4.3 Layer thickness effects

Figure 15 shows the distortions of the builds in the X+ and Y+ locations for the layer thickness ranging from 20-80 m. For the layer thickness 20um, 40um and 60um, the distortion does decrease, but the difference is very small about 0.2%-0.5% in average. This decreasing trend can be explained by the fact that increasing the layer thickness reduces the residual stress due to reduction in the cooling rate [49] [50]. Ali et al. [51] conducted experiments on three layer thicknesses (25 um, 50 um, and 75 um) and investigated their molten pools. It is reported that increasing layer thickness leads to decreasing cooling rates and increasing porosity. Meanwhile, the maximum molten pool temperature also increased due to the increasing layer thickness, thus the residual

stress and distortion were decreased according to the temperature gradient mechanism [52] and cool-down phase model [53].

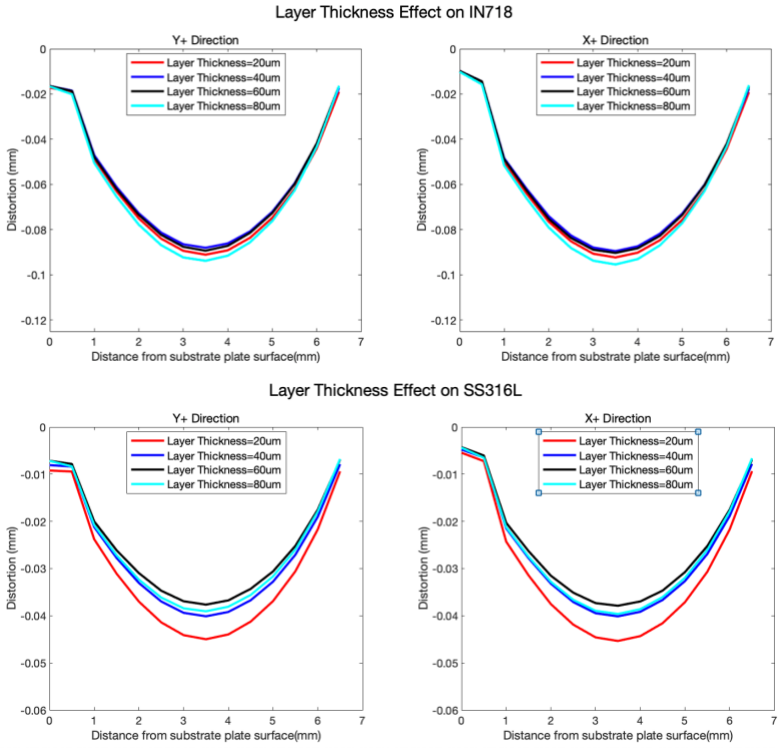


Figure 15. Distortion profiles for four layer thicknesses in AM.

### 4.4 Laser power effects

Figure 16 plots the distortion profiles under three laser powers, respectively. It can be seen that a higher laser power will lead to a larger distortion, which is due to the higher maximum temperature of molten pools [46], [54], [55], and higher cooling rates [46] and lower residual stress and distortion [56]. It is also important to have stable and desired molten pool characteristics during the printing process. It has been widely accepted that a reasonable combination of the laser power and scan speed will lead to efficient absorption of laser energy by the powder layer and sufficient depth of the molten pools to avoid lack of fusion voids [34], [52].

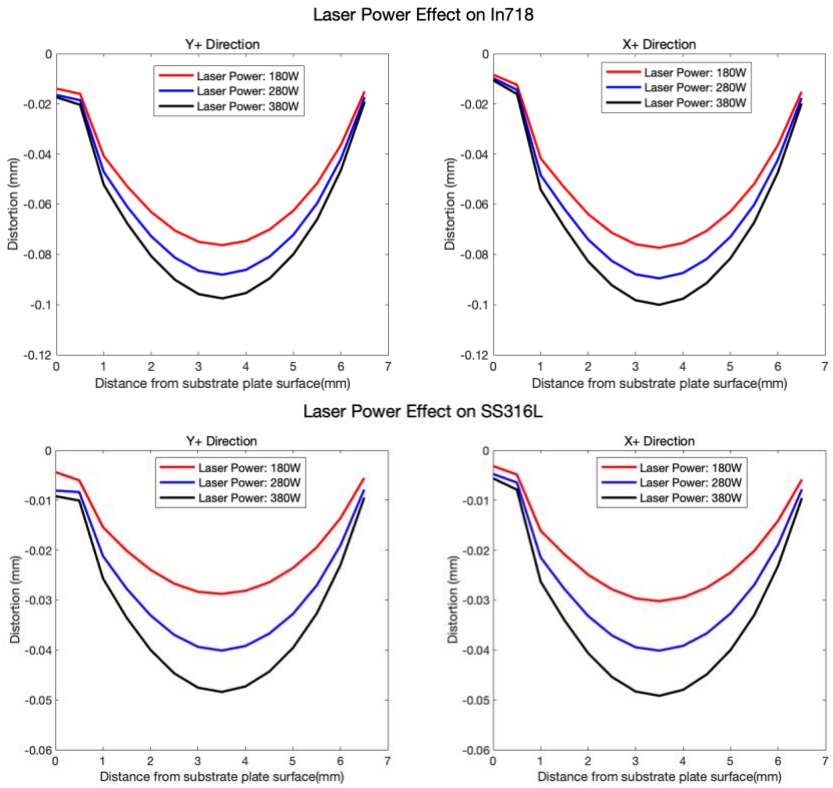


Figure 16. Distortion profiles for three laser powers under 40um layer thickness and rotating scan pattern.

Figure 17 (a) to (c) summarized all above parametric effects on maximum distortion of building model for both materials, giving us a direct comparison and conclusion that SS316L performs less distortion on final build than In718 for all ranged laser power, scan speed and layer thickness. The average improvement rates for maximum distortions stay around 50%.

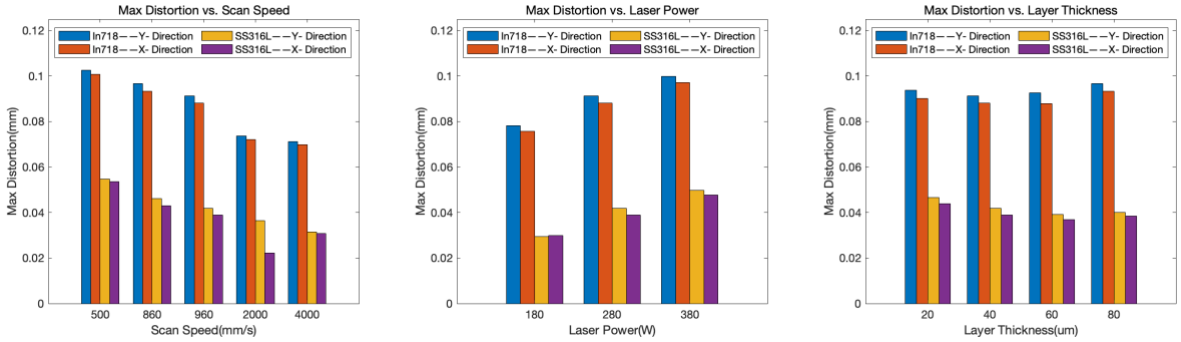


Figure 17. Maximum distortions versus (a) Scan speed. (b) Laser Power. (c) Layer thickness for both In718

and SS316L.

### 4.5 Material effects

Stainless steel 316L is a popular BP material for PEM fuel cell due to its mechanical robustness, corrosion resistance, and low cost. Figure 18 (a), (b) shows the distortion profiles using SS316L building material, indicative of similar deformation with the middle height subject to the largest deformation. It can be seen that the maximum distortion is much smaller than that of the In718 build with a value of 40 µm versus 90 µm in the two locations under same environment settings with In718. This is partially due to the smaller cooling rate and molten pool size in SS316L [34]. Note that 40 µm is still larger than or comparable to the membrane and catalyst layer thicknesses of PEM fuel cells, and may also lead to a large leakage under compressed operation conditions [57].

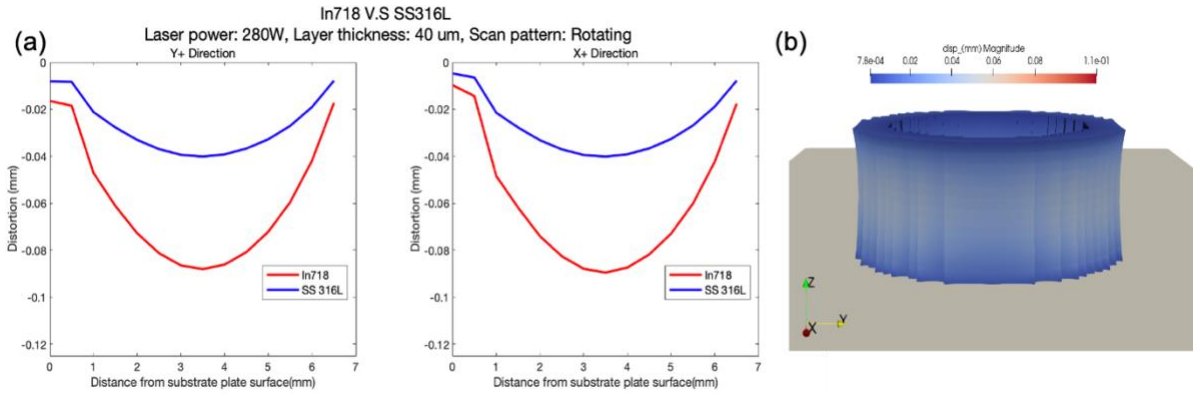


Figure 18. (a) Comparison of distortion using material SS316L and In718 under experiment parameters. (b) Predicted final geometry of case 1 using SS316L, with 10x magnified.

# Chapter 5: Molten pool characteristics

## 5.1 Implemented study of molten pool size

Like the welding process, residual stresses are produced in selective laser melting (SLM) processed part as the result of high temperature gradients, larger amount of thermal expansion and shrinkage and non-uniform plastic deformation during the heating and cooling cycle [49], [58], [59]. Substantial shrinkage of the moving melt pool during cooling and solidification is constrained by the cooler underlying previously processed layers [60]. The geometry of the melt track and the constitution of the melt pool significantly affects the dimensions of the final part. The melt pool stability is critical for the quality of SLM-fabricated parts; melt pool instability results in an irregular and discontinuous track, which leads to high surface roughness and volumetric porosity due to balling in the fabricated parts [26]. Given the fact that melt pool plays an essential role in affecting the simulation result, a single beam parametric simulation is implemented in AAS to obtain information about the melt pool characteristics of selected material, Inconel 718. In Figure 19, the melt pool information of the combination of 280 W and 960 mm/s is plotted along the bead after melt pool reached steady state. The convergence is reached within 0.3 to 0.5 mm. It also shows the full progression along the bead length and summary of average and median melt pool length, width, and reference depth for each permutation. One thing to be clear is that the reference depth is the entire melt pool depth minus the layer thickness, starts from the bottom of the first layer.

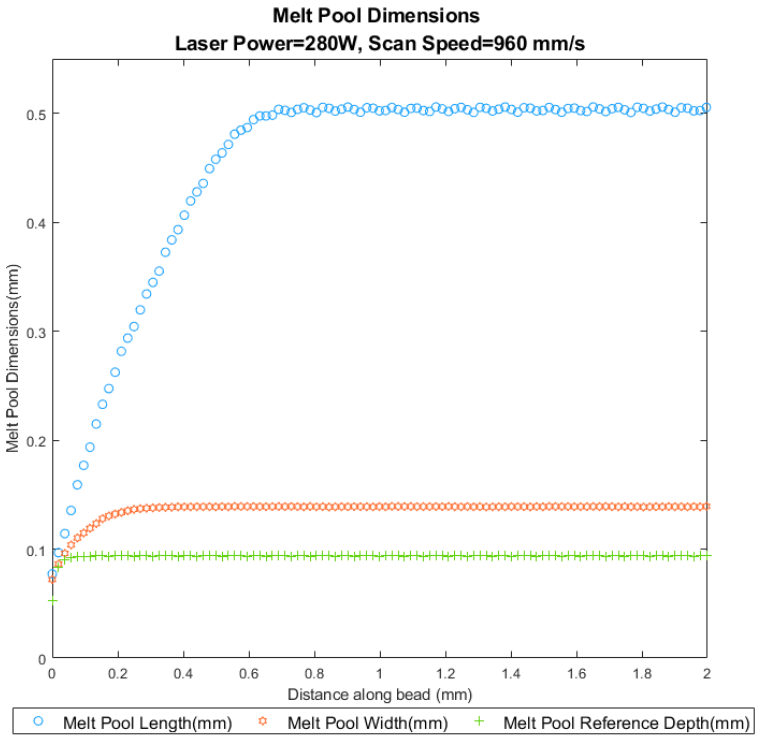


Figure 19. Melt pool dimension of experimental model.

### 5.2 Premutation analysis for porosity

As we have discussed in chapter 3. The effect of final build distortion for laser power is opposite with scan speed. Reducing laser power and increasing scan speed could both lead to lower residual stresses and distortions [56]. Thus, there must be a range for scan speed and laser power that interactively compromises to each other with a desirable neutralization for distortion. Figure 20 [52] summarizes such desirable combinations for these two parameters. In AAS we could also conduct a series of permutation analysis on a single layer to explore the approximate range of above-mentioned desirable window. Laser power is set between 80 to 430 in increment of 50, and scan speed is set between 560 to 1760 in increments of 200. These 8 laser powers and 7 scan speeds will have 56 different combinations with each other.

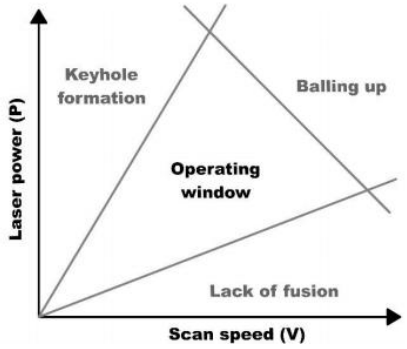


Figure 20. Laser power vs. scan speed plot: ideal operating window in AM [52].

To summarize these 56 permutations, we apply following three criteria to select proper combinations of laser power and scan speed [61]:

a). A penetration depth of about three layers through the thickness reduces porosity by re-melting previous layers, so that we want a melt pool depth that reaches at least halfway through the third layer. This means a good melt pool depth should be at least 0.1 mm, which leads to a melt pool reference depth larger than 0.06 mm. Otherwise, a lack-of -fusion would occur between the layers due to the high scan speed and low laser power.

b). A depth-to-width ratio above 0.95 indicates melt pools are too deep, and these permutations usually have low scan speeds and high laser power, which also means high energy density is applied and could lead to keyhole formation.

c). A length-to-width ratio below 4.0 indicates melt pools are too long that usually is the result of high scan speed and high laser power, which could potentially generate balling effect.

After selection based on above criteria, a chart summarizes all the combinations is shown in Figure 21. The five green points represent good candidates at the range of 130W to 230W and 760mm/s to 1160mm/s.

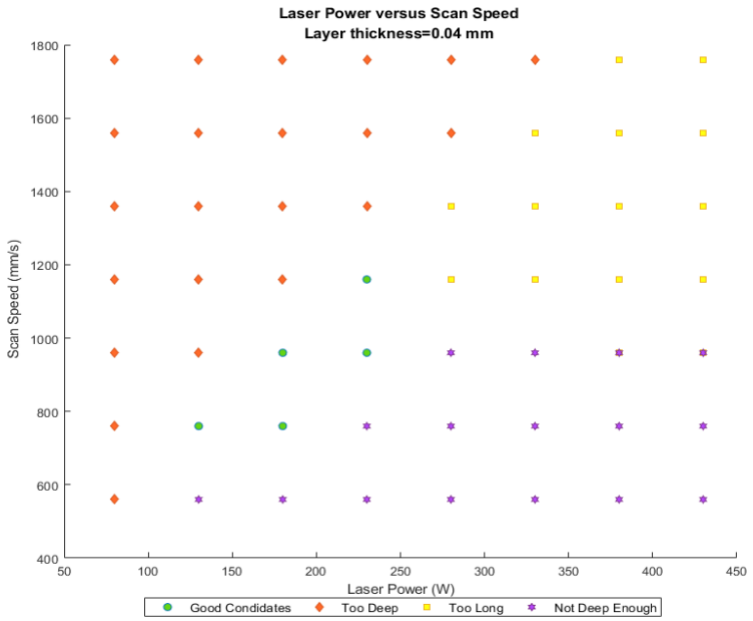


Figure 21. Result of different combinations of scan speed and laser power.

Porosity [62] is generally undesirable and considered as a material defect rather than a feature. Porosity has significance impact on LPBF parts, such as fatigue life. It could be produced by a variety of mechanisms including lack-of-fusion, keyhole-mode melting and gas absorption (i.e. Balling). Porosity parametric study is also available in AAS and it is usually the extension of material effect studies after single beam parametric simulation, it can offer more information about the level of porosity for the chosen printing material under different scan patterns. In above permutation studies, we get five candidates of combination of laser power and scan speed that are considered as good. In following study, more insight of porosity is implemented. To be noted, only lack-of-fusion porosity is considered and the criteria for result is solid ratio. An ideal solid would have a solid ratio of 1, and anything that is not a solid is a void or powder. We identify the best candidates as those have a less than 0.5% porosity and try to find the combination with the fastest scan speed and widest hatching spacing [61]. The simulation is executed for 130W, 180W and 230W at three scan speeds and five hatch spacings in table 6, the unqualified candidates for solid

ratio are abandoned.

We observe that lower scan speed will fix more hatch spacing values, and the same for increasing laser power. Combining these results with permutation study, a laser power of 230W with 960mm/s scan speed and a hatch spacing within 0.07mm to 0.11mm give us a more accurate result for the chosen material Inconel 718 in terms of proper melt pool size and less porosity.

**Table 6.** Summary of porosity results for the five good candidates.

| Laser Power (W) | | 130 | | | 180 | | | 230 | | |
|---|---|---|---|---|---|---|---|---|---|---|
| Scan Speed (mm/s) | | 760 | 960 | 1160 | 760 | 960 | 1160 | 760 | 960 | 1160 |
| Hatch Spacing (mm) | | Solid Ratio | | | Solid Ratio | | | Solid Ratio | | |
| | 0.07 | 1 | 0.9997 | 0.999 | 1 | 1 | 1 | 1 | 1 | 1 |
| | 0.09 | 0.999 | | | 1 | 1 | 0.9997 | 1 | 1 | 1 |
| | 0.11 | | | | 0.9997 | | | 1 | 0.9999 | 0.9991 |
| | 0.13 | | | | | | | 0.9995 | | |
| | 0.15 | | | | | | | | | |

Another thing to notice is, for the laser power 280W and scan speed 960mm/s that was used in pervious experiments and validations show a not deep enough melt pool based on Figure 21. However, this combination shows a better performance in lack-of-fusion porosity for wider parameter range, as shown in table 7.

**Table 7.** Porosity result for experiment and validation condition.

| Laser Power (W) | | 280 | | |
|---|---|---|---|---|
| Scan Speed (mm/s) | | 760 | 960 | 1160 |
| Hatch Spacing (mm) | | Solid Ratio | | |
| | 0.07 | 1 | 1 | 1 |
| | 0.09 | 1 | 1 | 1 |
| | 0.11 | 1 | 1 | 1 |
| | 0.13 | 1 | 0.9998 | 0.9962 |
| | 0.15 | 0.999 | | |

## Conclusion

In this study, we numerically investigated the distortions of LPBF builds of an inlet/outlet on a BP of fuel cells under various manufacturing parameters including the laser speed, laser scan pattern, laser power, build material, and powder layer thickness. The results of distortion prediction were validated again literature data for In718, in terms of distortion profiles at four locations for two geometries. The distortions at all measurement locations show a contraction toward the cylinder center for both cases. The maximum error rate compares with experiments is 10.4%, and average error rate is 8.4%. This could illustrate that the simulation in AAS performs an accurate prediction of distortion on building parts. Besides, the predicted geometries after build are also presented, giving a visualized idea of how residual stresses are distributed and accumulated in the building parts. In these cases, the maximum distortions occur at several layers below the top layer.

After the validation, a parametric study was carried out for both In718 and SS316L on the same building model together with few process parameters and their effects on final geometry. These parameters are scan speed, scan pattern, layer thickness and laser power. For each parameter, we have set control variable groups to present the changing distortion in certain range of parameter values. Two major factors are scan speed and laser power, that could cause a 12%-20% difference in distortions. Meanwhile, these are also two interactive variables that together decide an ideal operating window to avoid too much porosity (Lack of fusion, keyhole, balling) in LPBF. Moreover, we also prescribed the difference of resulted deformation between SS316L and Inconel 718, gives us the idea that different material types play an essential role in terms of building geometry as well. In this case, SS316L performs better than In718 under all changing configurations, which indicates its ability to be a more desirable chose to additively manufacture fuel cell components. To achieve manufacturing perfection and controlling cost loss in fuel cell

components, all above investigated parameters need to be considered comprehensively while each has interconnected effects on final building quality. AAS is a new package that released by ANSYS Inc. in 2019, related studies are still needed to examine the quality and accuracy.

Moreover, two implemented studies that focus on melt pool characteristics and porosity on a single layer were expanded in AAS as well. In these studies, numerical analysis was extensively conducted to explicate the features melt pools possessed. Under the condition of experimental validations, melt pool dimensions are captured. Meanwhile, after analyzing 56 combinations of different scan speeds and laser powers, a desirable operating window for these two values is obtained, giving more insights on selecting reasonable process parameters based on the ultimate need of building structures. Besides, one of the essential indices in LPBF—Porosity, is also studied. It helps to decide a solution based on all previous validations and porosity criteria including as many as parameters that involved in this LPBF for this fuel cell tube with material Inconel 718, that is 260W of laser power, 960 mm/s of scan speed, 0.07mm to 0.11mm of hatch spacing with reasonable scan pattern.

Above validations and investigations meant to provide a reference for all end-users and operators by using a size-suitable part and to inspire more potential applications for AM by this micro fuel cell component. The undesirable selection of material and process configurations could bring unnecessary time and economic loss as a consequence. Future studies may focus on exploring more combinations of different parameters and their effects on final geometries in multiple layers or bulk models that more than on a single layer.

## Reference


[1] Frazier, W. E. (2014). Metal additive manufacturing: a review. *Journal of Materials Engineering and performance*, *23*(6), 1917-1928.

[2] Murr, L. E., Gaytan, S. M., Ramirez, D. A., Martinez, E., Hernandez, J., Amato, K. N., ... & Wicker, R. B. (2012). Metal fabrication by additive manufacturing using laser and electron beam melting technologies. *Journal of Materials Science & Technology*, *28*(1), 1-14.

[3] Pitassi, D., Savoia, E., Fontanari, V., Molinari, A., Luchin, V., Zappini, G., & Benedetti, M. (2018). Finite element thermal analysis of metal parts additively manufactured via selective laser melting. *Finite Element Method—Simulation, Numerical Analysis and Solution Techniques*, 123-154.

[4] Zhang, X., McMurtrey, M. D., Wang, L., O'Brien, R. C., Shiau, C. H., Wang, Y., ... & Sun, C. (2020). Evolution of Microstructure, Residual Stress, and Tensile Properties of Additively Manufactured Stainless Steel Under Heat Treatments. *JOM*, 1-11.

[5] Wang, Y., Diaz, D. F. R., Chen, K. S., Wang, Z., & Adroher, X. C. (2020). Materials, technological status, and fundamentals of PEM fuel cells–a review. *Materials Today*, *32*, 178-203.

[6] Afshari, E., Mosharaf-Dehkordi, M., & Rajabian, H. (2017). An investigation of the PEM fuel cells performance with partially restricted cathode flow channels and metal foam as a flow distributor. *Energy*, *118*, 705-715.

[7] Liu, H., Qin, J., Rockward, T., Wu, J., Li, J., Li, G., ... & Shi, W. (2020). Photo-driven growth of a monolayer of platinum spherical-nanocrowns uniformly coated on a membrane toward fuel cell applications. *Journal of Materials Chemistry A*. DOI: 10.1039/D0TA07189G

[8] Song, Y., Zhang, C., Ling, C. Y., Han, M., Yong, R. Y., Sun, D., & Chen, J. (2020). Review on current research of materials, fabrication and application for bipolar plate in proton exchange membrane fuel cell. *International Journal of Hydrogen Energy*, *45*(54), 29832-29847.

[9] Adroher, X. C., & Wang, Y. (2011). Ex situ and modeling study of two-phase flow in a single channel of polymer electrolyte membrane fuel cells. *Journal of Power Sources*, *196*(22), 9544-9551.

[10] de Oliveira, M. C. L., Ett, G., & Antunes, R. A. (2012). Materials selection for bipolar plates for polymer electrolyte membrane fuel cells using the Ashby approach. *Journal of power sources*, *206*, 3-13.

[11] Wang, Y., & Feng, X. (2009). Analysis of the reaction rates in the cathode electrode of polymer electrolyte fuel Cells: II. Dual-Layer electrodes. *Journal of The Electrochemical Society*, *156*(3), B403.

[12] Wang, Y. (2009). Porous-Media Flow Fields for Polymer Electrolyte Fuel Cells: II. Analysis of Channel Two-Phase Flow. *Journal of the Electrochemical Society*, *156*(10), B1134.

[13] Afshari, E., & Houreh, N. B. (2015). Two-dimensional numerical modeling of a membrane humidifier with porous media flow field for PEM fuel cell. *International Journal of Modern Physics C*, *26*(06), 1550061.

[14] Park, J. E., Hwang, W., Lim, M. S., Kim, S., Ahn, C. Y., Kim, O. H., ... & Sung, Y. E. (2019). Achieving breakthrough performance caused by optimized metal foam flow field in fuel cells. *International Journal of Hydrogen Energy*, *44*(39), 22074-22084.

[15] Zhang, G., Wu, L., Jiao, K., Tian, P., Wang, B., Wang, Y., & Liu, Z. (2020). Optimization of porous media flow field for proton exchange membrane fuel cell using a data-driven surrogate model. *Energy Conversion and Management*, *226*, 113513.

[16] Bao, Z., Wang, Y., & Jiao, K. (2020). Liquid droplet detachment and dispersion in metal foam flow field of polymer electrolyte membrane fuel cell. *Journal of Power Sources*, *480*, 229150.

[17] Niu, Z., Wang, Y., Jiao, K., & Wu, J. (2018). Two-phase flow dynamics in the gas diffusion layer of proton exchange membrane fuel cells: volume of fluid modeling and comparison with experiment. *Journal of The Electrochemical Society*, *165*(9), F613.

[18] Carrere, P., & Prat, M. (2019). Impact of non-uniform wettability in the condensation and condensation-liquid water intrusion regimes in the cathode gas diffusion layer of proton exchange membrane fuel cell. *International Journal of Thermal Sciences*, *145*, 106045.

[19] Wang, Y., & Gundevia, M. (2013). Measurement of thermal conductivity and heat pipe effect in hydrophilic and hydrophobic carbon papers. *International Journal of Heat and Mass Transfer*, *60*, 134-142.

[20] Benner, J., Mortazavi, M., & Santamaria, A. D. (2018, November). Numerical Simulation of Droplet Emergence and Growth from Gas Diffusion Layers (GDLs) in Proton Exchange Membrane (PEM) Fuel Cell Flow Channels. In *ASME International Mechanical Engineering Congress and Exposition* (Vol. 52071, p. V06AT08A065). American Society of Mechanical Engineers.

[21] Wang, Y., Cho, S., Thiedmann, R., Schmidt, V., Lehnert, W., & Feng, X. (2010). Stochastic modeling and direct simulation of the diffusion media for polymer electrolyte fuel cells. *International journal of heat and mass transfer*, *53*(5-6), 1128-1138.

[22] Mishler, J., Wang, Y., Lujan, R., Mukundan, R., & Borup, R. L. (2013). An experimental study of polymer electrolyte fuel cell operation at sub-freezing temperatures. *Journal of The Electrochemical Society*, *160*(6), F514.

[23] Wang, Y., Pham, L., de Vasconcellos, G. P. S., & Madou, M. (2010). Fabrication and characterization of micro PEM fuel cells using pyrolyzed carbon current collector plates. *Journal of Power Sources*, *195*(15), 4796-4803.

[24] Buchbinder, D., Meiners, W., Pirch, N., Wissenbach, K., & Schrage, J. (2014). Investigation on reducing distortion by preheating during manufacture of aluminum components using selective laser melting. *Journal of laser applications*, *26*(1), 012004.

[25] Ansari, M. J., Nguyen, D. S., & Park, H. S. (2019). Investigation of SLM Process in Terms of Temperature Distribution and Melting Pool Size: Modeling and Experimental Approaches. *Materials*, *12*(8), 1272.

[26] Nozar, M., Zetková, I., & Hronek, O. (2018). Searching for favourable powder bed fusion settings in sintering of maraging steel ms1.

[27] Bikas, H., Lianos, A. K., & Stavropoulos, P. (2019). A design framework for additive manufacturing. *The International Journal of Advanced Manufacturing Technology*, *103*(9-12), 3769-3783.

[28] Leung, C. L. A., Marussi, S., Atwood, R. C., Towrie, M., Withers, P. J., & Lee, P. D. (2018). In situ X-ray imaging of defect and molten pool dynamics in laser additive manufacturing. *Nature communications*, *9*(1), 1-9.

[29] Martin, A. A., Calta, N. P., Khairallah, S. A., Wang, J., Depond, P. J., Fong, A. Y., ... & Tassone, C. J. (2019). Dynamics of pore formation during laser powder bed fusion additive manufacturing. *Nature communications*, *10*(1), 1-10.

[30] Gouge, M., Michaleris, P., Denlinger, E., & Irwin, J. (2018). The finite element method for the thermo-mechanical modeling of additive manufacturing processes. In *Thermo-Mechanical Modeling of Additive Manufacturing* (pp. 19-38). Butterworth-Heinemann.

[31] Rühmer, T. T., Gampe, U., Fischer, K. A., Wimmer, T., & Haberland, C. (2019, June). Structural Integrity Assessment and Engine Test of an Additive Manufactured First Stage Ring Segment of a Siemens Large Gas Turbine. In *Turbo Expo: Power for Land, Sea, and Air* (Vol. 58684, p. V07AT30A003). American Society of Mechanical Engineers.

[32] Maksimov, P., Smetannıkov, O., Dubrovskaya, A., Dongauzer, K., & Bushuev, L. (2018). Numeric simulation of aircraft engine parts additive manufacturing process. In *MATEC Web of Conferences* (Vol. 224, p. 01065). EDP Sciences.

[33] Mayer, T., Brändle, G., Schönenberger, A., & Eberlein, R. (2020). Simulation and validation of residual deformations in additive manufacturing of metal parts. *Heliyon*, *6*(5), e03987.

[34] Dunbar, A. J., Denlinger, E. R., Gouge, M. F., & Michaleris, P. (2016). Experimental validation of finite element modeling for laser powder bed fusion deformation. *Additive Manufacturing*, *12*, 108-120.

[35] Wang, Y., & Chen, K. S. (2013). *PEM fuel cells: thermal and water management fundamentals*. Momentum Press.

[36] Appleby, A. J. (1988). Fuel cell handbook.

[37] KYOGOKU, H., & IKESHOJI, T. T. (2020). A review of metal additive manufacturing technologies: Mechanism of defects formation and simulation of melting and solidification phenomena in laser powder bed fusion process. *Mechanical Engineering Reviews*, *7*(1), 19-00182.

[38] ASTM Committee F42 on Additive Manufacturing Technologies, & ASTM Committee F42 on Additive Manufacturing Technologies. Subcommittee F42. 91 on Terminology. (2012). *Standard terminology for additive manufacturing technologies*. Astm International.

[39] Zitelli, C., Folgarait, P., & Di Schino, A. (2019). Laser powder bed fusion of stainless steel grades: a review. *Metals*, *9*(7), 731.

[40] "INCONEL 718 TECHNICAL DATA," High Temp Metals, 2015. [Online].

[41] Zhang, L., Reutzel, E. W., & Michaleris, P. (2004). Finite element modeling discretization requirements for the laser forming process. *International Journal of Mechanical Sciences*, *46*(4), 623-637.

[42] Sun, C., Wang, Y., McMurtrey, M.D., Jerred N.D., Liou, F., Li, J. (2021). Additive manufacturing for energy: A review. *Applied Energy, 282.*

[43] Li, B. Q., Li, Z., Bai, P., Liu, B., & Kuai, Z. (2018). Research on surface roughness of AlSi10Mg parts fabricated by laser powder bed fusion. *Metals*, *8*(7), 524.

[44] Eidt, W., Tatman, E. P., McCarther, J., Kastner, J., Gunther, S., & Gockel, J. (2019). Surface roughness characterization in laser powder bed fusion additive manufacturing. In *Solid Freeform Fabrication Symposium*.

[45] Vasinonta, A., Beuth, J. L., & Griffith, M. (2007). Process maps for predicting residual stress and melt pool size in the laser-based fabrication of thin-walled structures.

[46] Manvatkar, V., De, A., & DebRoy, T. (2015). Spatial variation of melt pool geometry, peak temperature and solidification parameters during laser assisted additive manufacturing process. *Materials Science and Technology*, *31*(8), 924-930.

[47] Brückner, F., Lepski, D., & Beyer, E. (2007). Modeling the influence of process parameters and additional heat sources on residual stresses in laser cladding. *Journal of thermal spray technology*, *16*(3), 355-373.

[48] Ali, H., Ghadbeigi, H., & Mumtaz, K. (2018). Effect of scanning strategies on residual stress and mechanical properties of Selective Laser Melted Ti6Al4V. *Materials Science and Engineering: A*, *712*, 175-187.

[49] Kruth, J. P., Deckers, J., Yasa, E., & Wauthlé, R. (2012). Assessing and comparing influencing factors of residual stresses in selective laser melting using a novel analysis method. *Proceedings of the institution of mechanical engineers, Part B: Journal of Engineering Manufacture*, *226*(6), 980-991.

[50] Van Belle, L., Vansteenkiste, G., & Boyer, J. C. (2013). Investigation of residual stresses induced during the selective laser melting process. In *Key Engineering Materials* (Vol. 554, pp. 1828-1834). Trans Tech Publications Ltd.

[51] Ali, H., Ghadbeigi, H., & Mumtaz, K. (2018). Processing Parameter effects on residual stress and mechanical properties of selective laser melted Ti6Al4V. *Journal of materials engineering and performance*, *27*(8), 4059-4068.

[52] Mercelis, P. (2007). Control of selective laser sintering and selective laser melting processes.

[53] Shiomi, M., Osakada, K., Nakamura, K., Yamashita, T., & Abe, F. (2004). Residual stress within metallic model made by selective laser melting process. *CIRP Annals*, *53*(1), 195-198.

[54] Yadroitsev, I., Krakhmalev, P., & Yadroitsava, I. (2014). Selective laser melting of Ti6Al4V alloy for biomedical applications: Temperature monitoring and microstructural evolution. *Journal of Alloys and Compounds*, *583*, 404-409.

[55] Alimardani, M., Toyserkani, E., Huissoon, J. P., & Paul, C. P. (2009). On the delamination and crack formation in a thin wall fabricated using laser solid freeform fabrication process: an experimental–numerical investigation. *Optics and lasers in engineering*, *47*(11), 1160-1168.

[56] Wu, A. S., Brown, D. W., Kumar, M., Gallegos, G. F., & King, W. E. (2014). An experimental investigation into additive manufacturing-induced residual stresses in 316L stainless steel. *Metallurgical and Materials Transactions A*, *45*(13), 6260-6270.

[57] Wang, Y., Seo, B., Wang, B., Zamel, N., Jiao, K., & Adroher, X. C. (2020). Fundamentals, materials, and machine learning of polymer electrolyte membrane fuel cell technology. *Energy and AI*, 100014.

[58] Gu, D. D., Meiners, W., Wissenbach, K., & Poprawe, R. (2012). Laser additive manufacturing of metallic components: materials, processes and mechanisms. *International materials reviews*, *57*(3), 133-164.

[59] Mercelis, P., & Kruth, J. P. (2006). Residual stresses in selective laser sintering and selective laser melting. *Rapid prototyping journal*.

[60] Vrancken, B., Cain, V., Knutsen, R., & Van Humbeeck, J. (2014). Residual stress via the contour method in compact tension specimens produced via selective laser melting. *Scripta Materialia*, *87*, 29-32.

[61] ANSYS,Inc, “Additive User's Guide (Print and Science),” Canonsburg, PA, 2019.

[62] Ronneberg, T., Davies, C. M., & Hooper, P. A. (2020). Revealing relationships between porosity, microstructure and mechanical properties of laser powder bed fusion 316L stainless steel through heat treatment. *Materials & Design*, *189*, 108481.

## Appendix

The whole process of 3-dimensional numerical analysis in AAS is reviewed here. Following steps in Figure 22 shows the working flow in detail. In general, 12 steps are employed in above studies, and each of the step and its setting interface is presented using the validation case 1 as example for reproducibility and future research.

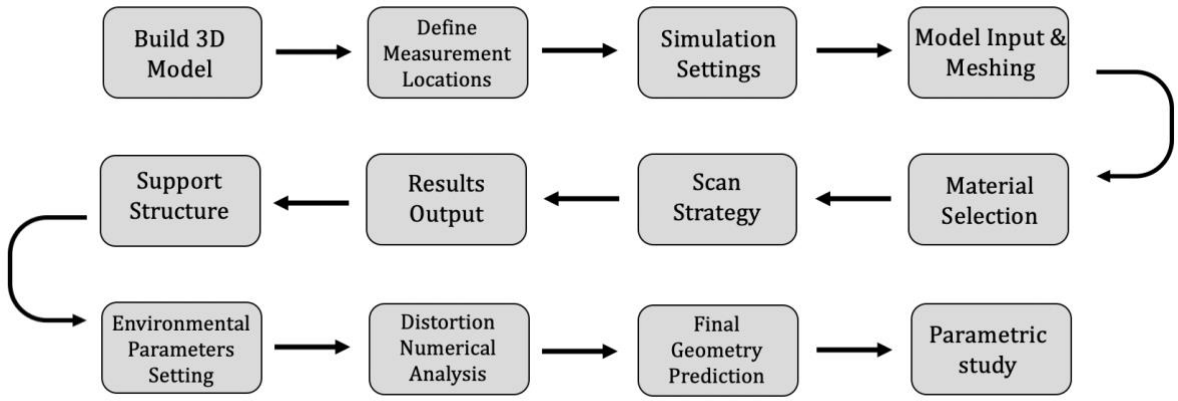


Figure 22. Steps of three-dimensional numerical analysis.

**Build 3D Model:** The desirable shapes and structures for AM simulation are able to be built in most 3-dimensional design tools, such as SolidWorks, Pro/E, Autodesk Invertor and the like. This study chose SolidWorks as design tool to obtain STL format files. To be noted, AAS and ANSYS workbench are separate platforms so that SpaceClaim and Design Modeler are not feasible for direct design and input of printing models into AAS like workbench does.

**Define Measurement Locations:** Measurement locations usually focus on area that has massive distortion or residual stress, it could be along a line, a surface or partial volume of the model. In our case, they are four lines along the contour of the cylinder height.

**Simulation Settings:** As Figure 23 shows, we select Thermal Strain Simulation in AAS that has the highest accuracy to predict thermal effect from melting and cooling cycles. Simulation

title can be anything as long as it clear for users. Number of cores ranges from 4-12, helps to divide the number of process core to be used, the maximum value was chosen in all our cases.

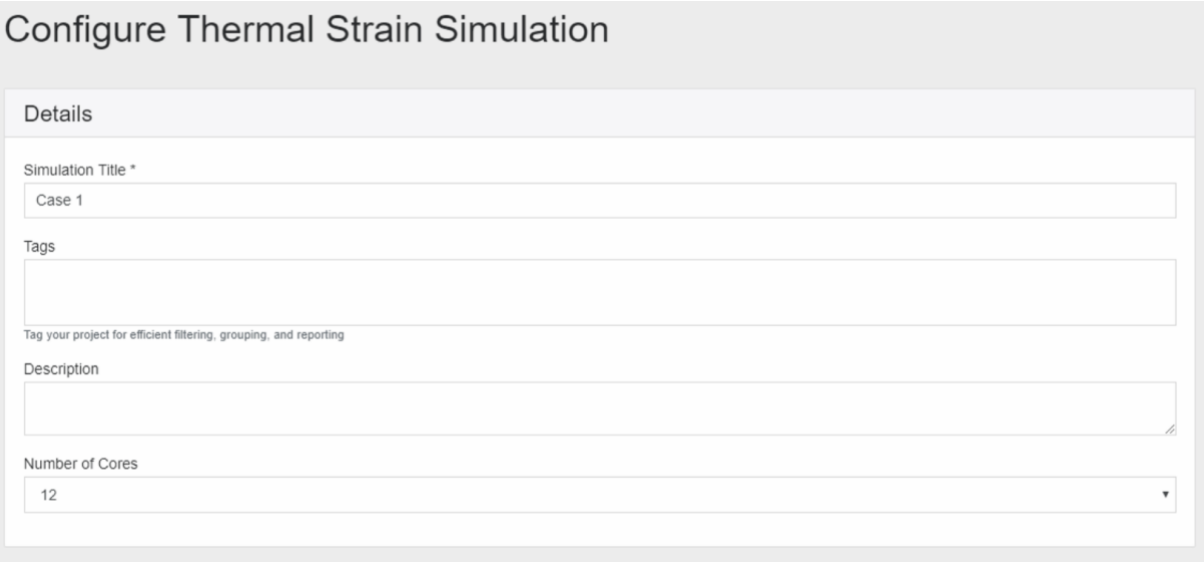


Figure 23. Configure thermal strain simulation. [61]

**Model Input & Meshing:** Like other finite element analysis, meshing size decides the accuracy and resolution ratio of final results after model input. In this stage, partial meshing control is not available yet in ASS, so meshing size is applied to entirety. Depending on computation resources, smaller meshing could capture part features as much as possible. Once add the part that needs to be calculated, voxel size and sample rate together decides meshing density. Here, default values for these are kept, more discussion about these concepts have investigated in Chapter 2.

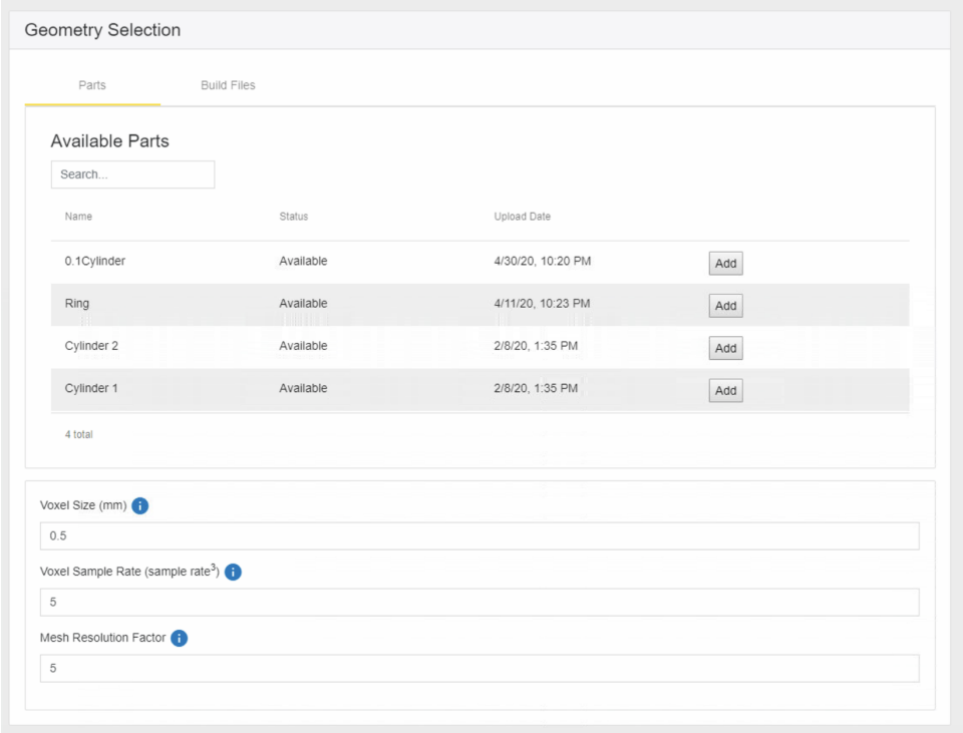


Figure 24. Geometry selection in AAS. [61]

**Support Structure:** Support is feasible to be user costumed (Input support model like the way inputting building models), and it will associate with building model. Also, support can be automatically generated if no special feature or overhang is concerned. Since the design of our case already has a substrate along with it, simulation with supports is unclicked in our study.

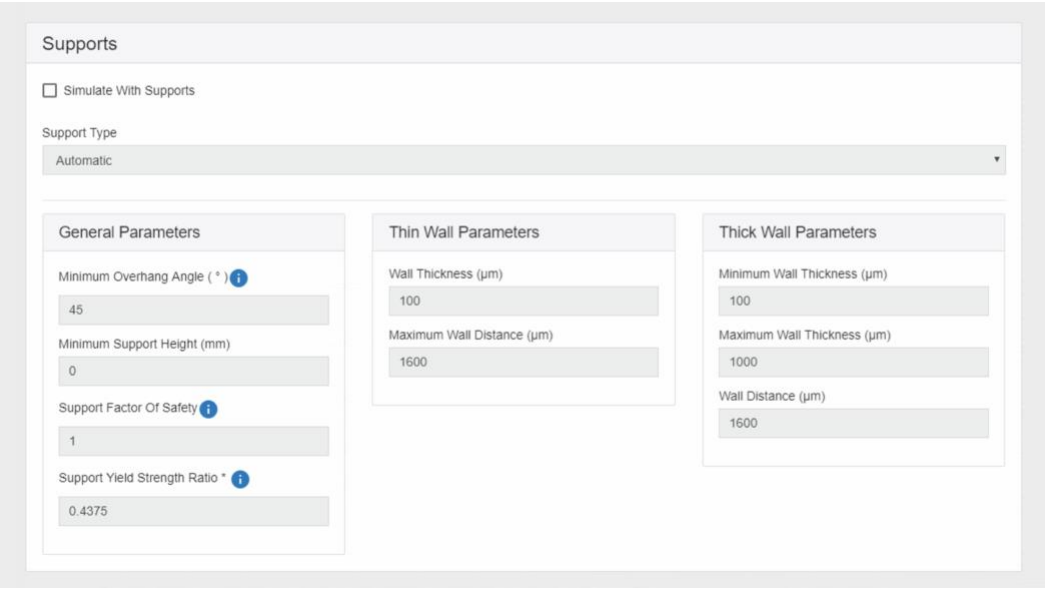


Figure 25. Support option in AAS. [61]

**Environmental parameters setting:** From this step, the model is already to be printed as long as configurations are decided. The initial temperature of the building environment, specifically, refers to the base temperature of the operation surface is set to default (room temperature).

**Material Selection:** In our case, IN718 and SS316L are selected from AAS material library, respectively, as shown below.

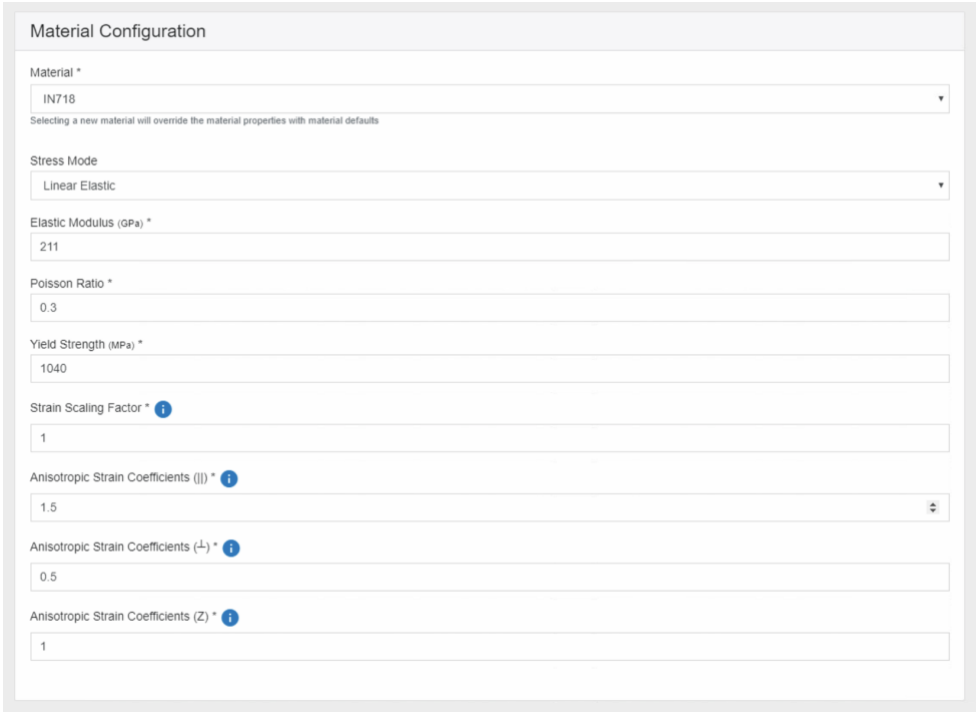


Figure 26. Material configuration in AAS. [61]

**Scan Strategy:** As we have talked in thesis, scan strategy includes all major variables (layer thickness, scan pattern, laser power, scan speed, hatch spacing, etc.) that brings different effect on building model, and they are the objects for parametric studies. Their effects that contribute to residual stress were also discussed. For the validation case 1, the values are given by the experiments and setup as shown in Figure 27.

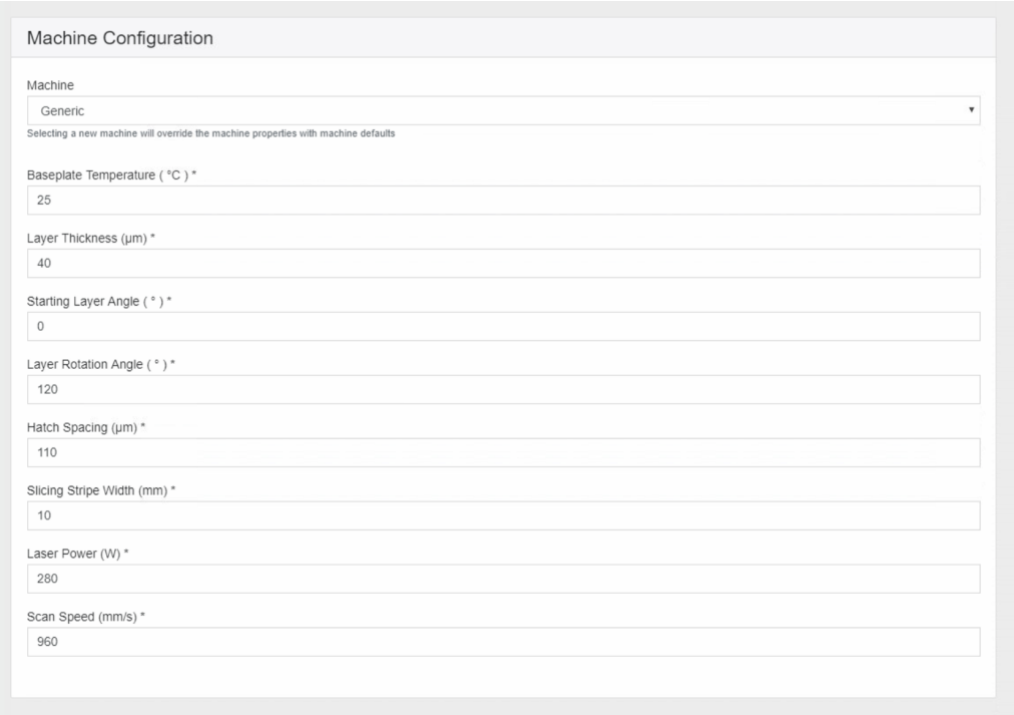


Figure 27. Machine configuration in AAS. [61]

**Results Output:** Most of FEA results for our study were produced in VTK files that include displacement before/after cutoff from support structure (if there is), layer-by-layer stress and displacement, etc. Our cases take the "before cutoff" results and convert them into visualized three-dimensional figures, and then **Distortion Numerical Analysis** for selected measurement locations and **Predicted Final Geometries.**

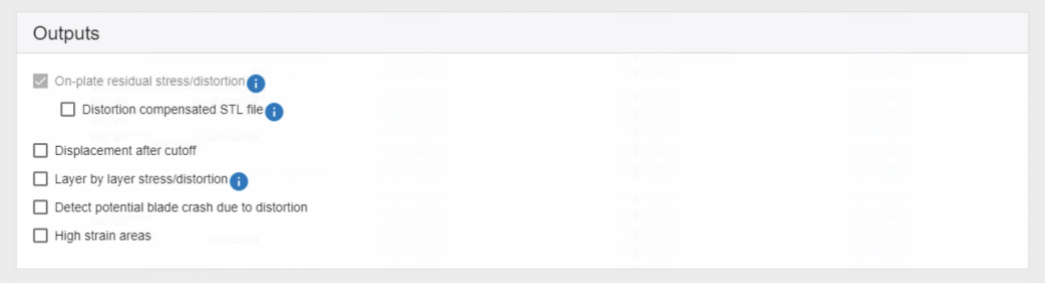


Figure 28. Result outputs in AAS. [61]

**Parametric Study:** Following the same steps, different settings of scan strategies are computed and processed into same presentation format.